EFDA–JET–PR(08)01

M.N.A. Beurskens, G. Arnoux, A.S. Brezinsek, C.D. Challis, P.C. de Vries, C. Giroud, A. Huber, S. Jachmich, K. McCormick, R.A. Pitts, F.G. Rimini, A. Alfier, E. de la Luna, W. Fundamenski, S. Gerasimov, E Giovannozzi, E. Joffrin, M. Kempenaars, X. Litaudon, T. Loarer, P. Lomas, J. Mailloux, R. Pasqualotto, V. Pericoli-Ridolfini, R.Pugno, E. Rachlew, S. Saarelma, E.Solano, M Walsh, L Zabeo, K.-D.Zastrow
and JET EFDA contributors

Pedestal and ELM Response to Impurity Seeding in JET Advanced Scenario Plasmas

Pedestal and ELM Response to Impurity Seeding in JET Advanced Scenario Plasmas

M.N.A. Beurskens[1], G. Arnoux[2], A.S. Brezinsek[3], C.D. Challis[1] P.C. de Vries[1], C. Giroud[1], A. Huber[3], S. Jachmich[4], K. McCormick[5], R.A. Pitts[6], F.G. Rimini[2], A. Alfier[7], E. de la Luna[8], W. Fundamenski[1], S. Gerasimov[1], E Giovannozzi[9], E. Joffrin[2], M. Kempenaars[1], X. Litaudon[2], T. Loarer[2], P. Lomas[1], J. Mailloux[1], R. Pasqualotto[7], V. Pericoli-Ridolfini[9], R.Pugno[5], E. Rachlew[10], S. Saarelma[1], E.Solano[8], M Walsh[1], L Zabeo[1], K.-D.Zastrow and JET EFDA contributors*

JET-EFDA, Culham Science Centre, OX14 3DB, Abingdon, UK

[1]EURATOM/UKAEA Fusion Association, Culham Science Centre, Abingdon, Oxon, OX14 3DB, UK
[2]Association EURATOM -CEA, CEA/DSM/DRFC-Cadarache 13108, St Paul Durance, France
[3]Assoziationen EURATOM -Forschungszentrum, J¸lich D- 52425 Jülich Germany,
[4]Association EURATOM-"Belgian State", ERM/KMS, Brussels, Belgium, Partner in the TEC,
[5]Association EURATOM-Max-Planck-Institut für Plasmaphysik, D-85748 Garching, Germany,
[6]Association EURATOM, Conférédation Suisse, EPFL, 1015, Lausanne, Switzerland,
[7]Consorzio RFX - Associazione Euratom-Enea, Corso Stati Uniti 4, I-35127, Padova, Italy,
[8]Laboratorio Nacional de Fusión, Asociación EURATOM-CIEMAT, Madrid, Spain,
[9]Associazione EURATOM -ENEA, ENEA Centro Ricerche Frascati C.P. 65, 00044 Italy,
[10]Association EURATOM-VR, Department of Physics, SCI, KTH, SE-10691 Stockholm, Sweden,
** See annex of M.L. Watkins et al, "Overview of JET Results ",*
(Proc. 21 st IAEA Fusion Energy Conference, Chengdu, China (2006)).

Preprint of Paper to be submitted for publication in
Nuclear Fusion

ABSTRACT

Advanced scenario plasmas must often be run at low densities and high power, leading to hot edge temperatures and consequent power handling issues at plasma-surface interaction zones. Experiments at JET are addressing this issue by exploring the use of extrinsic impurity seeding and D_2 puffing to reduce heat fluxes.

The experiments presented in this paper continue the line of Advanced Tokamak scenario studies at high triangularity in JET by concentrating on the characterisation of the edge pedestal and the ELM behaviour with Deuterium and/or light impurity fuelling (Neon, Nitrogen). Both injection of extrinsic impurities and D_2 puffing are shown to have a significant impact on the edge pedestal in typical JET Advanced Tokamak conditions. The ELM energy loss, $\Delta W_{ELM}/W_{dia}$, can be reduced to below 3% and the maximum ELM penetration depth can be limited to $r/a > 0.7$, thus enhancing the possibility for sustainable internal transport barriers at large plasma radius. These conditions can be achieved in two separate domains, either at a radiated power fraction (F_{rad}) of 30% or at a fraction of $> 50\%$. At the lower F_{rad} the ELMs are Type I and a high pedestal pressure is maintained, but the occasional large ELM may still occur. At $F_{rad} > 50\%$ the pedestal pressure is degraded by 30%-50%, but the ELMs are degraded to Type III. The intermediate regime at $F_{rad} \sim 40\%$ is unattractive for ITB scenarios because large Type I ELMs occur intermittently during the predominantly type III ELM phases (compound Type I/III). $F_{rad} = 30\%$, can be obtained with D_2 fuelling alone, whereas neon or nitrogen seeding is needed to achieve $F_{rad} > 50\%$. Only a limited number of tests have been carried out with nitrogen seeding, with the preliminary conclusion that the plasma edge behaviour is similar to that with neon seeding once the radiated fraction is matched.

1. INTRODUCTION

The optimisation of fusion performance in plasma scenarios characterised by Internal Transport Barriers (ITBs) has naturally led to experiments that combine the enhanced core confinement with a reduced edge transport, i.e. with an H-mode edge barrier [1, 2, 3]. Such an optimisation also requires that the ITB encloses a large plasma volume, i.e. the outer edge, or 'foot', be located at a relatively large radius [4]. Previous experiments at JET have shown that combining ITBs with ELMy edge conditions introduces specific challenges, particularly the need to avoid large ELMs that can have a detrimental effect on the internal barrier while, at the same time, retaining as much benefit as possible from the edge transport barrier and pressure pedestal. The cold pulse due to large periodic edge pedestal relaxations with Type I ELMs often penetrates deep into the plasma and can reach the foot of the ITB, causing a loss of the improved core confinement [5-10]. It is, therefore, advantageous to develop a plasma regime featuring 'small' ELMs, to minimise their effects on the ITB dynamics, whilst maintaining as high an edge pressure pedestal as possible.

At plasma-facing surfaces, particularly the divertor targets, severe constraints are being placed on the maximum plasma energy loss per ELM that can be tolerated in ITER [11]. An ELM energy loss limit of $\Delta W_{ELM} = 1$MJ has recently been set for the average ELM size based on materials

damage limits under laboratory exposure to transient plasma heat fluxes on timescales expected for ITER ELM energy deposition times. A 1MJ ELM represents an energy loss of only ~ 0.3% of the plasma stored energy for an ITER $Q_{DT} = 10$ burning plasma and is well below the smallest Type I ELM relative energy loss seen in today's devices (Q_{DT} = [output fusion power]/[input additional heating power]). Mitigation of ELMs is therefore mandatory in the next step. In addition, material erosion places limits on the average inter-ELM heat flux which is acceptable for ITER (~10MW/m^2 [12]). In the absence of an intrinsic carbon source in ITER (in the event of an all-metal first wall option being chosen), extrinsic impurities will be required to achieve the radiative divertor regime necessary to achieve partial divertor detachment and hence limit the peak steady state heat fluxes.

To test the chosen ITER wall material mix, JET is preparing an ambitious upgrade, the ITER-Like Wall project (ILW) [13]. This will provide an all Beryllium main chamber wall with tungsten divertor plates and will be accompanied by a substantial increase in additional heating power and duration. The development of scenarios with mitigated transient and steady state power loads has thus now become a matter of considerable importance within the JET experimental programme.

Previous JET experiments have demonstrated that ELMs can indeed be "passively" mitigated (i.e. as opposed to forced mitigation techniques such as pellet pacing [14] or magnetic field line ergodisation [15,16]) by seeding noble gases like argon and krypton in ITB plasmas with low triangularity ($\delta \sim 0.25$-0.3). In these cases the ITB could be sustained for several confinement times [4, 5]. More recently, JET experiments have also been performed to develop Advanced Tokamak (AT) scenarios approaching the ITER relevant triangularity of $\delta \sim 0.4$. Despite the achievement of AT scenarios at high triangularity on JT-60U [17], the initial JET results have shown that maintaining ITBs is more difficult than at low triangularity due to changes in the edge pedestal and ELM characteristics [7, 8, 9]. It was subsequently demonstrated that ITBs could be sustained in JET at $\delta \sim 0.4$-0.5 with careful control of the plasma edge using deuterium and/or impurity injection [10]. More specifically, it was shown that in plasmas with a combination of D_2 and neon injection, an ITB could be triggered and sustained for ten energy confinement times at a radius of $r/a \sim 0.8$ in a plasma with $\delta \sim 0.4$ and $q_{95} \sim 7.5$ and without significant impurity accumulation. In these plasmas the total radiated power was 50-55% of the input power, with significant edge cooling and a reduced pedestal pressure. The large, low frequency, type I ELMs typical of the unfuelled scenario were replaced by either much smaller high frequency type I ELMs, type III ELMs, or even an L-mode edge.

The experiments described here build on the findings reported in [10] and are aimed specifically at the development of a high triangularity, AT scenario H-mode edge at an ITER relevant $q_{95} \sim 5$ compatible with the power handling requirements of the planned ILW. To reduce transient ELM loads and minimise ELM induced ITB perturbation, such a scenario must operate with the highest pedestal pressure compatible with reduced ELM amplitude and demonstrate adequate heat flux dissipation at the divertor targets without unacceptable core plasma impurity contamination [18, 19, 20]. The aim of this particular set of experiments was edge pedestal behaviour characterisation rather than attempting to trigger and sustain strong Internal Transport Barriers (ITBs), since the

ITB dynamics can easily complicate a systematic investigation of edge behaviour by introducing a time-dependent variation in the loss power from the plasma core [8]. This study concentrated, instead, on exploring, without an ITB, the possible edge parameter space where ELMs could be compatible with both ITB formation and the power handling constraints that will be imposed by the ILW. The seeding gasses used in this study were D_2, Ne and N_2, a choice based on the encouraging results in [10] and the successful use of N_2 in JET for edge cooling, and subsequent ELM mitigation, in conventional ELMy H-mode and so-called 'hybrid' scenarios in JET [21, 22].

This paper is structured as follows: Section 2 describes the high triangularity plasma scenario and the impurity seeding technique used; Section 3 describes the effect of impurity seeding on ELM characteristics and Section 4 its impact on pedestal parameters and pedestal profiles. The pedestal dynamics during an ELM, and the potential impact of the ELMs on an ITB are discussed in Section 5. Finally, a discussion of the implications of this work for AT scenario development, and conclusions for future experiments are given in Section 6.

2. IMPURITY SEEDING IN A HIGH TRIANGULARITY AT-SCENARIO

The JET MarkIIHD divertor with new Load Bearing Septum Replacement Plate (LBSRP) [23] enables high triangularity plasmas ($\delta \sim 0.45$) with a larger volume than was previously possible [10]. Figure 1 shows the high triangularity configuration that was used for this study. The plasmas in these experiment were run at a toroidal magnetic field of 3.1T and a plasma current of roughly 2MA, corresponding to $q_{95} \sim 5$. The line averaged density was typically in the range of $4\text{-}5\times10^{19}$ m^{-3}, corresponding to 60-80% of the Greenwald density, and typical of the relatively low density conditions of most of the AT scenarios at JET.

Apart from the requirement to obtain high triangularity, the choice of magnetic configuration for these experiments is largely driven by the constraints set by the future ILW. The ILW divertor geometry will be largely unchanged from the configuration shown in figure 1, but the current CFC vertical target tiles will be replaced by W coated CFC units and the CFC LBSRP will be exchanged for a solid W target.

The combination of toroidal geometry and poloidal drifts are known to produce strong asymmetries favouring the outer target in the in-out divertor power deposition for normal field direction [19, 24], particularly at high power (as in the discharges described here). Since the solid W LBSRP presents the best power handling capability the outer strike point is thus positioned on this surface. To achieve the high triangularity, the inner strike point must, however, be placed high on the vertical tiles, leading to an asymmetric strike point geometry with short X-point-to-target connection lengths on the inboard side and longer distances at the outboard. This in turn produces additional heat load asymmetries such that the preferential outer target loading can be somewhat reduced. As a consequence of the planned W coated vertical tiles, it may thus turn out to be the case that the inner strike zone imposes the highest restrictions on the compatibility of these AT scenarios with the ILW.

Figure 2 shows the time evolution of the main plasma parameters for a typical discharge. The total combined input power ($P_{tot} = P_{NBI} + P_{ICRH} + PW$) for the plasmas in the experimental series was between 20 and 25MW. The heating scenario was chosen to provide a target q-profile for the main high power phase with low core magnetic shear and $q_0 > 1$, the so-called 'Optimised Shear' regime on JET. Variations in Ptot are provided mainly by changes in the injected ICRF power due to different ICRH coupling in the various H-mode regimes.

The gas seeding in these experiments was applied in feedforward mode, i.e. a pre-programmed waveform was used to control the gas injection. A series of impurity seeding gas puffs were applied at a rate of 2Hz, since even at the lowest required level of continuous neon seeding (the equivalent of 5.10^{20} electrons/s) the gas valves could not be operated reliably. However, because the neon diffusion rate into the pedestal region has a time constant of ~ 0.5s (i.e. of the order of the modulation frequency), the introduction of gas in this way did not affect the resulting ELM behaviour. The various gas injection modes used in these experiments may be summarised as follows, in order of increasing level of radiated power:

1. Unfuelled reference discharges, with no additional D_2 or impurity injection. These were used to probe the effect of machine conditioning on plasma behaviour.
2. Deuterium-only discharges, with a base level of D_2 gas seeding of $3.5.10^{21}$ electrons/s and featuring higher frequency ELMs than in an identical unfuelled case.
3. Impurity-seeded discharges, with a varying level of either N_e (5.10^{20}–2.10^{21} electrons/s) or N_2 (5.10^{21}–2.10^{22} electrons/s) seeding. The majority of these discharges were Ne seeded.
4. Impurity and deuterium discharges, with a seeding combination of either N_e (1.10^{21} electrons/s) or N_2 ($1.5.10^{22}$ electrons/s) with D_2 ($1.5.10^{22}$ electrons/s).

The JET vertical bolometry lines of sight have been used to quantify the radiated power level. The bolometry signals represent a base-line in between ELMs with superimposed intermittent radiation spikes caused by the ELMs. The baseline level represents the condition during which the ELMs are triggered, and this radiated power in between ELMs is used in the characterisation of ELMs versus radiation level. By synchronising the bolometry signal to the ELM timing inferred from the D_α signal a very accurate base line radiated power between ELMs can be calculated.

Figure 3(a) shows the evolution of the total radiated level (in between ELMs) for the bulk and x-point/divertor region of the JET plasmas as a function of the total radiated power in between ELMs. Ideally these signals would be obtained from time resolved tomography of the vertical and lateral bolometry line of sights on JET. However, as the ELM frequency in this experiment varies from 30 to ~ 250Hz, this is not possible for the entire range observed in this paper. (A fast tomography algorithm that can select the baseline signal in fast ELMing plasmas is under construction.) Instead, two sets of vertical bolometry lines of sight have been used (Figure 1.) These signals have been compared to ELM resolved tomographic reconstructions of the Bulk ($r/a<0.95$) and the divertor X-point radiation for lower ELM frequencies in this study and have been found to be in good agreement within 5% of the radiated power.

The total radiated power fraction between ELMs varies from 15 to 65%. With low impurity injection rates the bulk radiated power dominates, but a saturation is observed at higher levels of Ne impurity seeding, between $F_{rad,total}$ of 45 and 65%. The X-point/divertor radiation, on the other hand, increases more than linearly when the total radiated fraction is increased by N_e seeding. N_2 seeding does not seem to feature any saturation of the bulk radiation.

A Ne injection location scan was performed by introducing gas from one of three different injection locations (see Figure 1): Gas Injection Module (GIM) 11, into the divertor Private Flux Region (PFR); the top of the main chamber (GIM5); and the outer divertor (GIM 9). Of the three locations, injection into the PFR was found to be most efficient, leading to the same level of radiated power for 30% less gas influx (in terms of electrons/s) compared with injection from GIMs 5 and 11). As shown in Figure 3, however, the ratio of radiated power from the bulk plasma compared to level of radiation from the divertor/X-point region was similar for all three injection locations. In summary, it was found that similar plasma conditions could be achieved regardless of the choice of injection location.

Based on the results obtained with Ne and the limited experimental time available, N_2 injection was attempted only from the PFR (GIM 11). Nitrogen was found to have a far lower fuelling efficiency than Neon, requiring an order of magnitude higher influx to obtain the same level of radiated power. This may be attributed to the chemical reactivity of N_2 with the carbon first wall surfaces [25]. Figure 3 shows that there are some slight differences between the two types of impurities in terms of location of the radiating regions. For the same level of total radiated power, N_2 seeding produces a higher relative radiation level in the Divertor/X-point radiation than Ne injection. The fact that N_2 has a relatively higher divertor/X-point radiation than Ne could be beneficial for mitigating transient and steady power loads in the divertor.

Throughout the experimental series the total net Power into the Scrape Of Layer or SOL, ($P_{net} = P_{tot} - P_{rad,bulk} - dW_{dia}/dt$) remains roughly constant because more efficient coupling of the ICRH power with smaller ELMs was compensated by the increased radiated power at higher levels of impurity seeding as can be seen in Figure 4.

3. ELM MITIGATION THROUGH IMPURITY INJECTION

Reference discharges without gas injection were used regularly during the experimental sessions to assess any effect of varying machine conditions and highlight possible ‘memory effects’ due to the impurity seeding in previous pulses on ELM behaviour. Figure 5 shows the D_α time traces for some of the reference discharges, all of which feature ELMs with characteristics that suggest their classification as type I. Some minor variations in ELM frequency (30-50Hz) and amplitude were observed, but the range of these differences is small compared with the effect of the impurity seeding on the ELM characteristics observed in the remainder of these experiments.

An overview of the ELM behaviour observed in this series of gas seeding experiments is given in Fig.6. This is a qualitative observation and ELM classification will be discussed in the next

paragraph. There is a clear change from ~30Hz Type I ELMs in the reference discharge without gas seeding to high frequency, possibly Type I, ELMs with D_2 only and low rate Ne seeding. With higher rates of N_e seeding a transition occurs to the so-called compound Type I/III ELMs, characterised as infrequent large ELMs followed by bursts of higher frequency small ELMs. At even higher seeding levels the compound character disappears and only small Type III ELMs are left with increasing frequency as the gas levels increase. At Frad above 50% high frequency ELMy H-modes and L-mode discharges are both possible. N_2 seeding has a similar effect on the ELMs.

The ELM frequency for all discharges in this experimental series is plotted as a function of total radiated power fraction between ELMs in Figure 7. The question of ELM classification in AT scenarios is not straightforward and it deserves some attention, since it is generally acknowledged that one cannot simply translate what is found in low q_{95} standard ELMy H-modes to the AT H-modes at higher q_{95}, one of the possible reasons being the differences in the edge pedestal stability with different current profiles [8, 9]. In JET AT scenarios, for example, the L-H power threshold is generally found to be higher in similar conditions that in sawtoothing H-modes [4], and type III ELMs can be observed at power levels significantly higher than twice the L-H power threshold. Classification of ELM-type is usually carried out by studying ELM frequency variations as a function of input power. As in this dataset the net input power does not vary significantly between pulses this classification is not possible here. As a first approach no distinction is made in ELM type and the total ELM frequency is plotted (ELM frequency = [Number of any type of ELM in a time window]/[duration of this time window]). It is likely that the first branch of frequency increase corresponds to type I ELMs with increasing frequency during gas fuelling, e.g. the transition from F_{rad} = 15% to 30% in Fig. 6. The subsequent drop in ELM frequency is caused by the occurrence of compound ELMs, i.e. mixed type I/type III ELMs with brief ELM free periods (e.g. F_{rad} = 42% in Fig.6). The second branch of increasing ELM frequency is likely to be a transition to Type III regime (e.g. F_{rad} = 50% in Fig.6), with a subsequent transition to L-mode. In this data set the transition from type III ELM to L-mode regimes occurs in the range of high radiated power fractions of Frad ≥ 50%. Although the number of discharges with nitrogen seeding is limited, Figure 6 also illustrates that for the same Frad, the ELM behaviour does not appear to depend on the injected gas species.

4. PEDESTAL ANALYSIS AND ENERGY CONFINEMENT.

Figure 8 and 9 shows the $T_e - n_e$ diagram and the pedestal electron temperature, density and pressure versus the radiated fraction respectively. The ELM characterization proposed in section 3 appears to be confirmed by the data trends in Fig.9. During the type I ELM phase the edge pedestal pressure is not strongly affected by the increase in radiated power fraction, whereas a clear edge pressure deterioration occurs after the onset of the phase of compound Type I/III ELMs. In the Type I ELMy H-mode regime the increase in electron density due to increased gas fuelling is compensated by a corresponding decrease in pedestal electron temperature such that the electron pressure remains roughly constant. Above F_{rad} = 40% the pedestal confinement decrease is likely to be associated

with a transition from Type I to type III ELMs and, eventually, a return to an L-mode regime. The confinement loss found here at F_{rad} = 40% is consistent with the results found at a transition from type I to III ELMs in standard ELMy H-modes [36].

High spatial resolution profiles of T_e, n_e and p_e are shown in Fig.10. These are obtained from the newly installed JET High Resolution Thomson Scattering (HRTS) system [26]. The edge profiles from this diagnostic are of such a high quality, that the edge pressure degradation as a function of increasing radiated fraction is seen very clearly. Edge stability analysis with the ELITE code [28, 29, 30] has been carried out for the first time using HRTS data: the bootstrap current profile for the experimental equilibrium was calculated self-consistently using bootstrap current calculation from [31] and HRTS density and temperature profiles in the HELENA equilibrium code [32]. In the code it was assumed that $p_i = p_e$, as the spatial resolution of the JET ion temperature diagnostics is insufficient for this stability analysis. The bootstrap current dominates the inductively driven current in the edge region, and therefore the HRTS measurements are indispensable for the edge current determination. Resistive modes are not included in the modelling. The numerical results indicate that at F_{rad} = 17% the plasma is marginally unstable to peeling-ballooning modes, whereas at F_{rad} = 42% and 60% the edge is in the stable domain (Fig.11(a)).

The edge stability analysis of standard Type I ELMy H-modes typically finds them to be close to the peeling-ballooning instability boundary [30], i.e. occupying the top right corner of the stability diagram (an example of which is given in Figure 11(a)) where current limited peeling modes meet the pressure limited ballooning instabilities. We can, therefore, consider the results of the ELITE code modelling for our high pedestal cases to support their classification as Type I ELMs.

As the plasmas in this experiment do not have any significant core confinement enhancement or ITBs the global confinement is expected to be determined by the pedestal confinement. Figure 12 shows the global energy confinement time relative to the IPB98(y,2) thermal scaling [33]. The thermal stored energy was estimated from the diamagnetic measurement, corrected for the calculated fast ion component. The confinement H-factor is below unity for all discharges in this experiment and HIPB98(y,2) ~ 0.85 for the unfuelled discharges. Usually unfuelled sawtoothing high triangularity Type I ELMy H-modes, at lower q_{95} than our dataset, have HIPB98(y,2) ≈ 1 [34]; the lower H-factor observed in the our experiments could be due to the choice of a q-profile, with q>1 in the core. Such an explanation would be consistent with recent observations in unfuelled high β_N (~3) JET experiments at high triangularity and q_{95} ~ 5, where the minimum value of q (qmin) was varied at the start of the main heating pulse thus revealing a degradation in the global confinement as q-min was raised from 1 to 2 [35]. However, another explanation could lie in the fact the inner divertor leg is close to the divertor tile. As a consequence, the increased recycling reaching the LCF acts as an additional fuelling source causing even the unfuelled discharges to have a slightly degraded HIPB98(y,2) < 1.

In the experimental series discussed in this paper, an initial decay is observed in the confinement H-factor with F_{rad} due to increasing gas fuelling. This is followed by a phase with constant HIPB98(y,2) until the confinement is degraded further at F_{rad} ~ 40-50%, at the transition from Type

I to Type III ELMs. In figure 12 the data set used in the analysis of this paper (P_{tot} = 20-25MW) is indicated by the black dots. A limited number of discharges that achieved higher input power of Ptot~30MW are indicated in figure 12 with red diamonds. Globally they follow the same trend as the lower power case, with the exception of the region of $F_{rad} > 50\%$. There is however no sign of improved core confinement for this group of discharges. The results show however that the pedestal degradation for these discharges is partly avoided thanks to the higher input power.

5. PEDESTAL DYNAMICS AND ITB COMPATIBILITY

The pedestal analysis in section 4 and the ELM characterization presented in section 3 show clearly that gas and impurity injection can effectively be used in a JET AT scenario to produce a whole spectrum of ELM types, from Type I ELMs to compound Type I/III ELMs to pure Type III ELMs and finally L-mode. However, one of the main aims of our study is to determine whether ELMs are compatible with ITB sustainment and reasonable wall power loading; it is, therefore, useful to classify the various ELMs in terms of ELM energy loss and effect on the plasma core. For this reason an analysis strategy has been developed using the available diagnostic data and combining ELM averaging techniques with individual ELM analysis to provide measures of the comparative impact of different ELM regimes.

The diamagnetic measurements are not sufficiently accurate in terms of signal to noise to determine the energy loss of each individual ELM for the entire range of ELM frequencies, at least for the higher frequency Type I ELMs, and certainly Type III events. Instead the energy loss is inferred from the electron temperature loss per ELM (using ECE measurements), which is cross-correlated with the ELM averaged stored energy drop. The co-linearity of these quantities is illustrated in Figure 13. The drop in pedestal temperature for individual ELMs varies from 10 to 500eV for all the ELMs in this experimental series (Figure 13 shows ELM averaged data, which explains the smaller range 0-200eV in that graph). Rather than trying to classify the ELM Types the ELMs are sorted into the following three categories: small ELMs with $\Delta T_e < 75$eV, large ELMs with $\Delta T_e <$ 75eV, and the largest ELM for each discharge. Figure 14 shows the ELM frequency, or average ELM occurrence per second, for 'small' and 'large' ELMs. The choice of $\Delta T_e = 75$eV as a selection criterion for ELM size is arbitrary, but a sensitivity study carried out with criterions of $\Delta T_e = 50$eV and $\Delta T_e = 100$eV shows very similar trends.

Figure 14 shows that 'large ELMs' occur up to a radiated power fraction of ~45%, after which only 'small ELMs' occur. Figures 15(a), (b), and (c) compile the dependence on Frad of pedestal T_e drop, relative plasma energy loss and ELM affected area for three ELM groupings: 'small', 'large' and 'largest'. Note that in the case of the 'small' and 'large ELM' groups, the data are averaged over several ELMs, whereas the 'largest ELM' represents the ELM with the largest Te-drop in the used time window. At low radiated power fractions the average ELM amplitude for 'large ELMs' is $<\Delta T_e>$~250 eV and $<\Delta W_{ELM}> = 5\text{–}6\%$ of W_{dia}; A local minimum occurs at $F_{rad} \sim 30\%$ where reduced values are found of $<\Delta T_e>$~150 eV and $<\Delta W_{ELM}> \sim 3\%$ of W_{dia}; At $F_{rad} \sim 40\%$ the averaged ELM

amplitudes are below these at low radiated power fractions (i.e. $<\Delta T_e> \sim 200$ eV and $<\Delta W_{ELM}>$ ~5% of W_{dia}), but occasional very large ELMs of $\Delta T_e \sim 400$eV are observed (compound Type I/III). 'Large ELMs' are not observed at $F_{rad} > 50\%$. It is clear that the character of 'small ELMs' is relatively independent of radiated power fraction and that they remain benign over the entire range, with $<\Delta T_e>$~25 eV and $<\Delta W_{ELM}> <1\%$.

The potential impact of the ELMs observed in this experiment on ITBs is illustrated in figure 15(c). Here the average and maximum ELM penetration depth is shown, expressed as the radius at which the drop in the local electron temperature due to the ELM, measured using ECE, is greater than 10% of the pre-ELM value, which corresponds to the measurement uncertainty. The ELM penetration depth follows the same trend as ΔT_e and ΔW_{ELM}. At $F_{rad} = 30\%$ even the largest ELMs do not penetrate further than r/a = 0.7, whereas at $F_{rad} = 15$-20% and $F_{rad} = 40\%$, ELMs are found to penetrate as deep as r/a = 0.5-0.6. Above $F_{rad} = 50\%$ the ELM penetration is very shallow and is restricted to a radius of r/a >0.9

Not all the ELMs regimes identified above are likely to be compatible to the formation and sustainment of ITBs at r/a = 0.6-0.7. As found in [7,10] large Type I ELMs are not compatible with ITBs at large plasma radius in JET. Therefore, one can conclude that two regimes are identified in the experiments reported in this paper which may be compatible ITB formation at large plasma radius:

- At $F_{rad} = 30\%$ with 'small' Type I ELMs, (r/a)penetration >0.7 and $\Delta W_{ELM}/W_{dia} <3\%$.
- At $F_{rad} > 50\%$ with Type III ELMs, (r/a)penetration>0.9 and $\Delta W_{ELM}/W_{dia} <1\%$.

At a radiated fraction of 30% the pedestal pressure is maintained at the same high level as for the unfuelled type I ELMy cases, although the occasional ELM still penetrates as deep as r/a = 0.7. At $F_{rad} > 50\%$ ELM penetration becomes peripheral, but the pedestal pressure is typically reduced by at least 25% (Fig.9). On the other hand the 'large ELMs' found at $F_{rad} = 15$-30% and $F_{rad} = 40\%$ are likely to be unacceptable for ITB formation at large radius. Figure 16 shows the distribution function of ELM penetration depth for the two cases of $F_{rad} = 30\%$ and 40%. It is possible to envisage that ITBs might recover from an occasional 'large' ELM, but at $F_{rad} = 40\%$ they become relatively frequent (6-10 ELMs per second). In contrast no deeply penetrating ELMs (further in than r/a = 0.7) occur at $F_{rad} \sim 30\%$, hence operation at this value of F_{rad} seems to present a more favourable condition for ITB formation and sustainment.

DISCUSSION AND CONCLUSIONS

Within the framework of the scientific effort presently being devoted to the preparation of a viable AT scenario for steady-state operation of high Q_{DT} tokamak devices, a thorough exploration has been carried out at JET of the possible use of impurity seeding to achieve moderated ELM activity compatible with a high confinement ITB. These experiments are even more crucial in view of significantly reducing the power and energy load, both transient and stationary, to plasma facing

components and to ensure the survival of metal walls, envisaged for future devices.

In the experiments considered in this paper it has been found that both extrinsic impurities and D_2 puffing can have a significant impact on the edge pedestal in AT relevant scenarios at relatively low density ne of 60-80% of the Greenwald density. $\Delta W_{ELM}/W_{dia}$ can be reduced to below 3% and the maximum ELM penetration depth can be limited to r/a>0.7, thus enhancing the possibility for sustainable ITBs at large plasma radius. These conditions can be achieved in two separate scenarios, either at F_{rad} = 30% or F_{rad}> 50%. At the lower F_{rad} a high pedestal pressure is maintained, but the occasional large ELM may still occur. At F_{rad} >50% the pedestal pressure is degraded by at least 25%, but no large, deeply penetrating ELMs are observed. The intermediate regime of compound Type I/III ELMs at F_{rad} ~ 40% is unattractive for ITB scenarios because large Type I ELMs occur intermittently during the predominantly type III ELM phases. Only D_2 fuelling is required to achieve F_{rad} = 30%, whereas neon or nitrogen seeding is needed to achieve F_{rad} >50%. Although tests have been less extensive than with neon, for a given radiated fraction, nitrogen seeding appears to yield similar pedestal and ELM dynamics as observed with neon.

The peak transient power load to the wall is also greatly reduced in the regimes identified above as “good” with respect to ELMs-ITBs compatibility, which is an important consideration in view of the ablation threshold of the wall material, i.e. beryllium or tungsten in the JET ITER-like wall. However, the time averaged power load in these plasmas due to ELMs stays roughly constant up to the radiation fraction where the Type I to Type III transition takes place, i.e. at F_{rad} = 50%.

The results presented in this paper represent a first step towards the development at JET of an Advanced Tokamak scenario fully compatible with operation in an all-metal wall environment. It is clear that there are additional issues that have not been tackled yet, like minimisation of localised fast ion energy losses in the main chamber, operation at high density and its effect on ITB triggering and formation and, last but not least, the requirement to replace the intrinsic carbon impurity once the ITER-like wall is installed. The ILW installation will, also, be accompanied by a substantial upgrade of the JET additional heating power [26], which will require an extrapolation of the results obtained at the 25-30MW level to ~ 45MW of total power. This will call for a more in-depth understanding of the physics and atomic processes underlying the various ELMs regimes observed in our experiments to guide, for example, in the choice of extrinsic impurity to be used.

A possible concern for extrapolation to future JET experiments is the narrowness, in terms of F_{rad}, of the region around F_{rad} ~ 30% where good pedestal confinement combines with limited radial penetration of the cold pulse at the ELM crash. If this finding is confirmed by further experiments, planned for the 2008 JET campaign, a more sophisticated approach will have to be devised, for example using real-time feedback control of the radiated power fraction, as already developed at JET in the so-called “hybrid” scenario [22].

The question of the role of ELMs with respect to the formation and the sustainment of ITBs remains open. The experiments reported here have significantly expanded the operational space for AT scenarios in terms of radial ELM penetration depth and edge scenarios have been developed

specifically to be compatible with ITBs located at large radius. However, a full integration of the edge regimes established here with the maximum available heating power, optimal current profile and core confinement improvement has still to be done.

ACKNOWLEDGEMENT

This work was partly supported by the UK Engineering and Physical Sciences Research Council and by the European Communities under the contract of Association between EURATOM and UKAEA. The views and opinions expressed herein do not necessarily reflect those of the European Commission. This work was partly conducted under the European Fusion Development Agreement.

REFERENCES

[1]. Gohil P. et al Plasma Phys. Control. Fusion (2002) **44** A37.
[2]. Litaudon X. et al Plasma Phys. Control. Fusion (2006) **48** A1.
[3]. Kamada Y. et al Plasma Phys. Control. Fusion (2006) **48** A419–A427.
[4]. Gormezano C. et al. Plasma Phys. Control. Fusion **41** (1999) B367–B380.
[5]. Becoulet A. et al Nucl. Fusion (2000) **40** 1113.
[6]. Sips A.A.C. et al Nuclear Fusion (2001) **41**, No. 11.
[7]. Crisanti F. et al Plasma Phys. Control. Fusion (2003) **45** 379.
[8]. Sarazin Y. et al Plasma Phys. Control. Fusion (2002) **44** 2445.
[9]. Becoulet M. et al Plasma Phys. Control. Fusion (2003) **45** A93.
[10]. Rimini F.G. et al Nucl. Fusion (2005) **45** 1481.
[11]. Pitts R.A. et al, 49th APS Division of Plasma Physics Meeting, Orlando, Florida USA, 2007.
[12]. Loarte A. et al.; Power and particle control, Nucl. Fusion **47** (2007) S203.
[13]. Paméla J., et al Journal of Nuclear Materials **363–365** (2007) 1–11.
[14]. Lang P.T., et al Nucl. Fusion **44** (2004) 665–677.
[15]. Evans T.E., et al Journal of Nucl. Mat. V**337-339** (2005) 691-696.
[16]. Liang Y. et al., Phys. Rev. Lett. **98** (2007) 265004.
[17]. Fujita et al, 2002 Nucl. Fusion **42** 180–186.
[18]. Litaudon X. et al, et al, accepted for publication in Plasma Phys. Control. Fusion 2007.
[19]. Arnoux G. et al, 34th EPS Conf on Plasma Physics, Warsaw, Poland, 2007.
[20]. Jachmich S. et al, 34th EPS Conf on Plasma Physics, Warsaw, Poland, 2007.
[21]. Rapp J. et al Nucl. Fusion **44** (2004) 312–319.
[22]. Corre Y. et al, 34th EPS Conf on Plasma Physics, Warsaw, Poland, 2007.
[23]. Paméla J. et al 2003 Fusion Engineering and Design, **66-68** 25-37.
[24]. R.A. Pitts et al., J. Nucl. Mater **337-339** (2005) 146.
[25]. F.L. Tabarés et al., J. Nucl. Mater. **337-339** (2005) 867-871.
[26]. Ciric D., et al, 23rd SOFT Conference, Venice, Italy, 2004.
[27]. Pasqualotto R, et al Rev. Sci. Instrum. (2004) **75**, 3891.

[28]. Wilson H.R., Snyder P.B., et al Phys Plasmas **9** (2002) 1277.
[29]. Snyder P.B.,Wilson H.R., et al., Phys. Plasma**s 9** (2002) 2037.
[30]. Snyder P.B.,Wilson H.R., et al., Nucl. Fusion **44** (2004) 320.
[31]. Sauter O. et al Physics of Plasmas (1999) V6-N7 2834.
[32]. Saarelma S. et al Plasma Phys. Control. Fusion (2005) **47**, 713.
[33]. IPB Editors; Plasma confinement and transport, Nucl. Fusion(1999) **39**, 2175.
[34]. Saibene et al. Plasma Phys. Control. Fusion **44** (2002) 1769–1799.
[35]. Challis et al, 34th EPS Conf on Plasma Physics, Warsaw, Poland, 2007.
[36]. SartoriR., et al. Plasma Phys. Control. Fusion **46** (2004) 723–750.
[37] Mailloux J. et al, 34th EPS Conf on Plasma Physics, Warsaw, Poland, 2007.

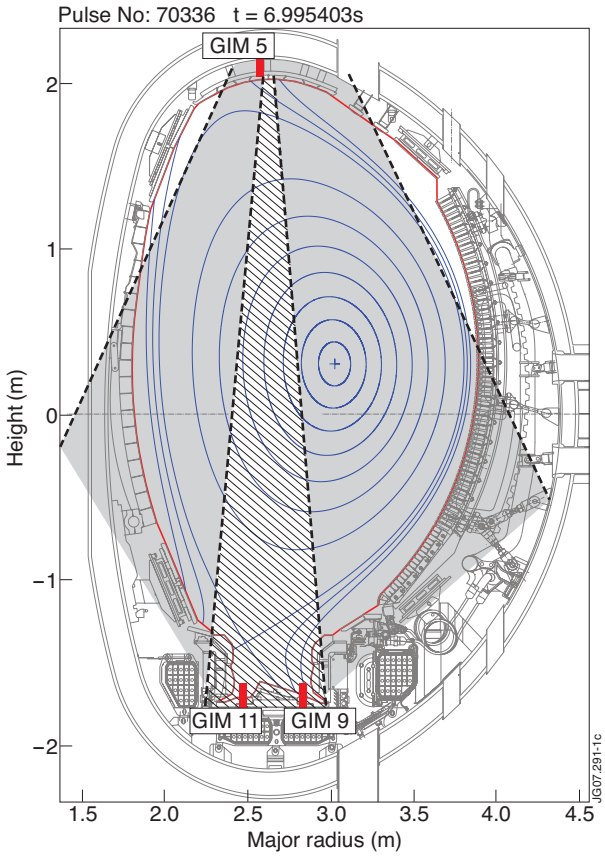

Figure 1: High Triangularity configuration used for the edge characterisation experiments. The outer strikepoint was placed on the load bearing septum replacements plate, which will have the highest power handling in the ILW. The gas injection locations for N_e are indicated as GIM5, GIM9 and GIM11. N_2 was injected from GIM11 only. The shaded areas indicate the viewing areas of the bolometer for respectively the "Divertor and X-point" region (hashed) and the "Bulk plasma" region (grey) as used in Figure 3.

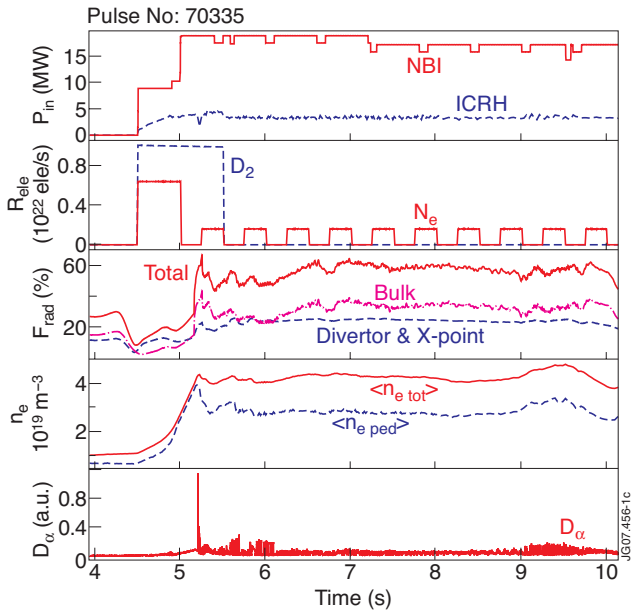

Figure 2: Typical waveforms for the impurity seeding experiments. P_{tot} ~ 20MW (=P_{NBI}+P_{ICRH}+P_{Ω}). Feed-forward neon injection waveform with 0.25s puffs and average injection ~ 10^{21} electrons/s. The radiated fraction is the base line of bolometry measurements ($F_{rad,total}$ = $F_{rad,\ diveror}$+ $F_{rad\ Bulk}$= 35%+25%). Core and edge electron density (from interferometry) remained steady during the phase of constant ELM behaviour (6.2-9s)

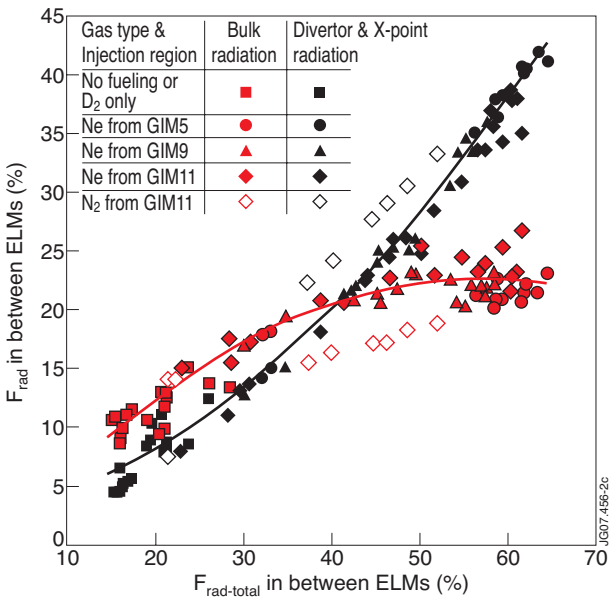

Figure 3: Divertor & X-point (black) and bulk (red) versus total radiated fraction (F_{rad} = P_{rad}/P_{tot} in percent) between ELMs for all discharges in this experiment (star symbols: N_2, other symbols: D_2 and/or N_e). The radiated power was obtained from selected viewing lines of the bolometer array ($F_{rad,total}$ = $F_{rad,divertor}$+ $F_{rad,bulk}$). The symbols indicate the gas injection location: Squares: no impurity injection, diamonds: divertor private flux region, circles: top of main chamber, and triangles: bottom of main chamber. The lines represent parabolic fits to the divertor & X-point and bulk radiation fractions, respectively, for the combined D_2 and Ne seeded data.

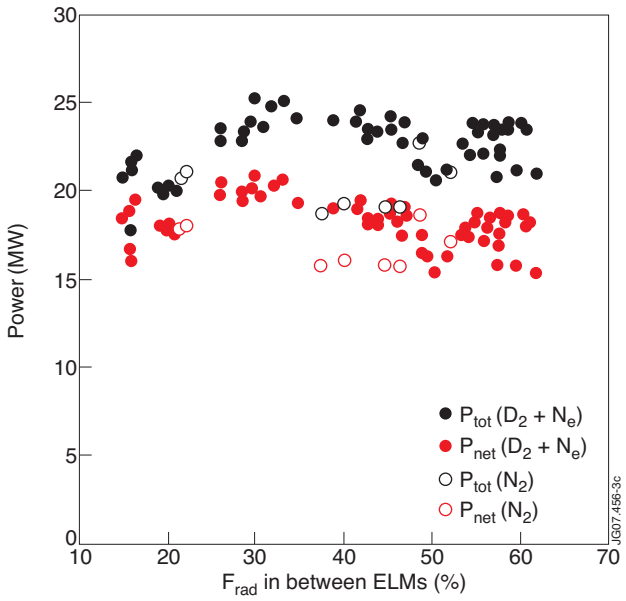

Figure 4: Total input power (blue) and net power into the SOL, P_{net}=P_{tot}-$P_{rad,bulk}$-$dW_{dia/dt}$, (red) as a function of (total) radiated fraction for the plasmas in this experiment. Although the input power increases as the radiated fraction increases from 15 to 30% as a result of the improved coupling of the ICRH power as the ELM size decreases, the net power into the SOL remains roughly constant for the entire range of radiated fractions. Closed symbols are for D_2 and N_e seeded discharges, open symbols for N_2 seeded discharges.

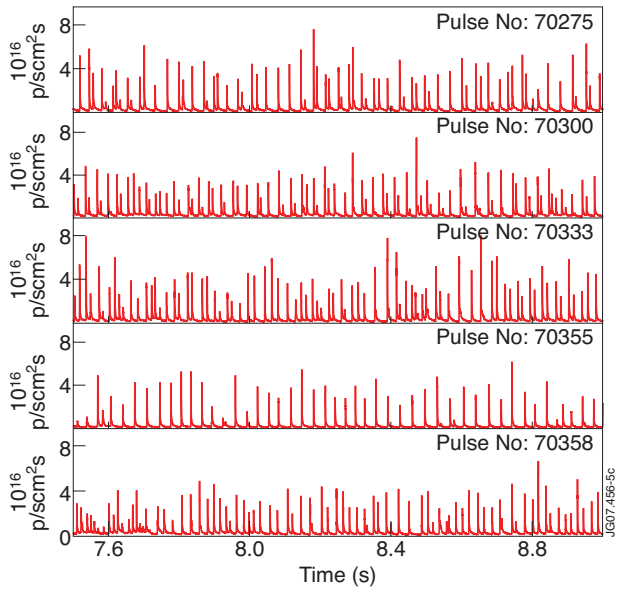

Figure 5: D_α time traces from the outer divertor view for all reference discharges without gas fuelling. The radiated fraction of these discharges is between 15 and 20%.

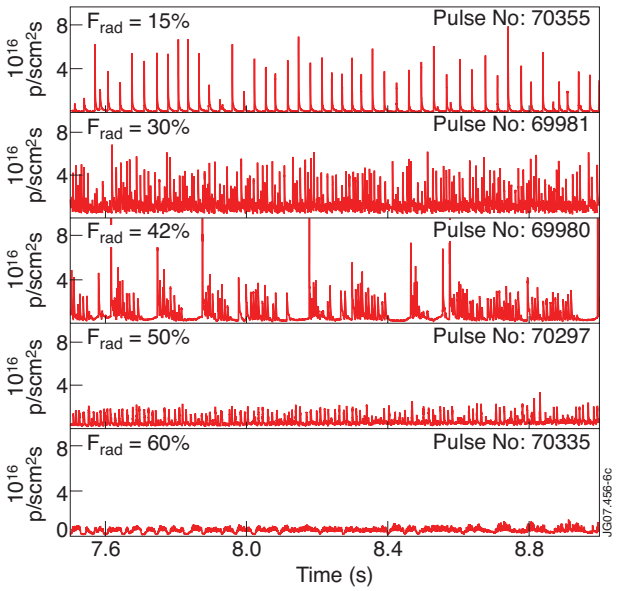

Figure 6: D_α time traces from the outer divertor view for discharges with increasing N_e seeding with radiative fraction of respectively 15% (no gas), 30% (D_2+N_e), 42% (D_2+N_e), 50% (D_2+N_e), and 60% (D_2+N_e). In these examples, D_2 seeding was kept constant alongside the N_e seeding.

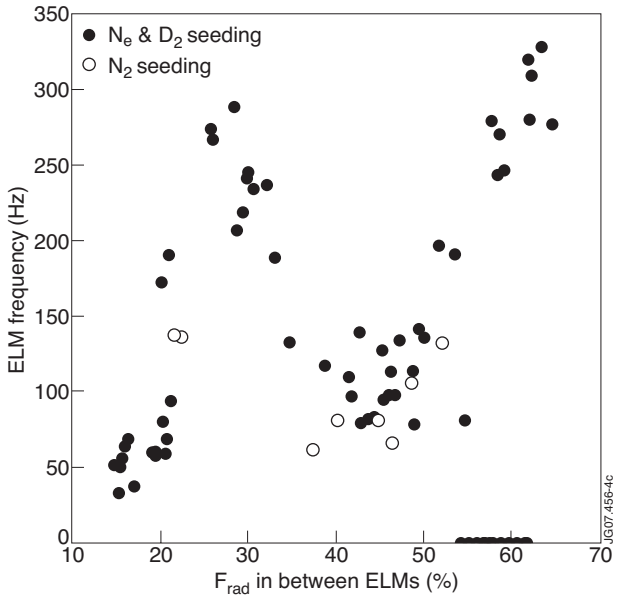

Figure 7: ELM frequency as a function of F_{rad}. Open symbols are nitrogen seeded plasmas. Note that above F_{rad} ~55% L-mode discharges occur with zero ELM-frequency.

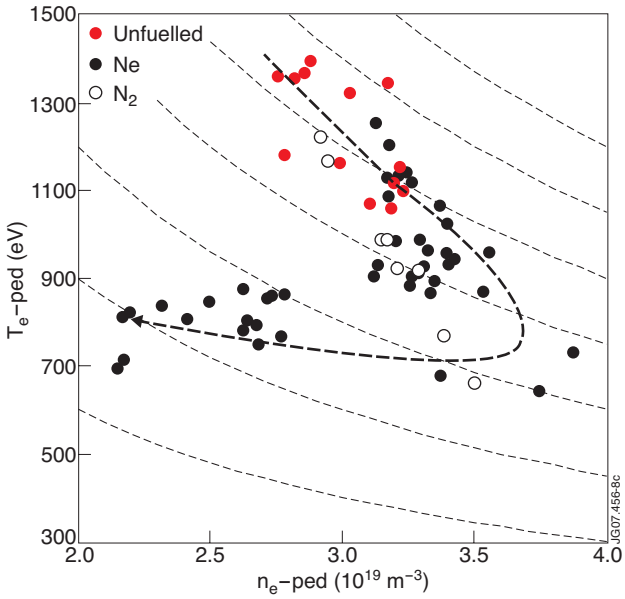

Figure 8: Electron pedestal T_e–n_e diagram for the discharges in this experiment. Pedestal T_e -is derived from ECE measurements at r/a=0.9 and the pedestal n_e measurement is obtained from line integrated interferometry measurements. The arrow indicates increasing levels of F_{rad}. The hashed lines are isobars.

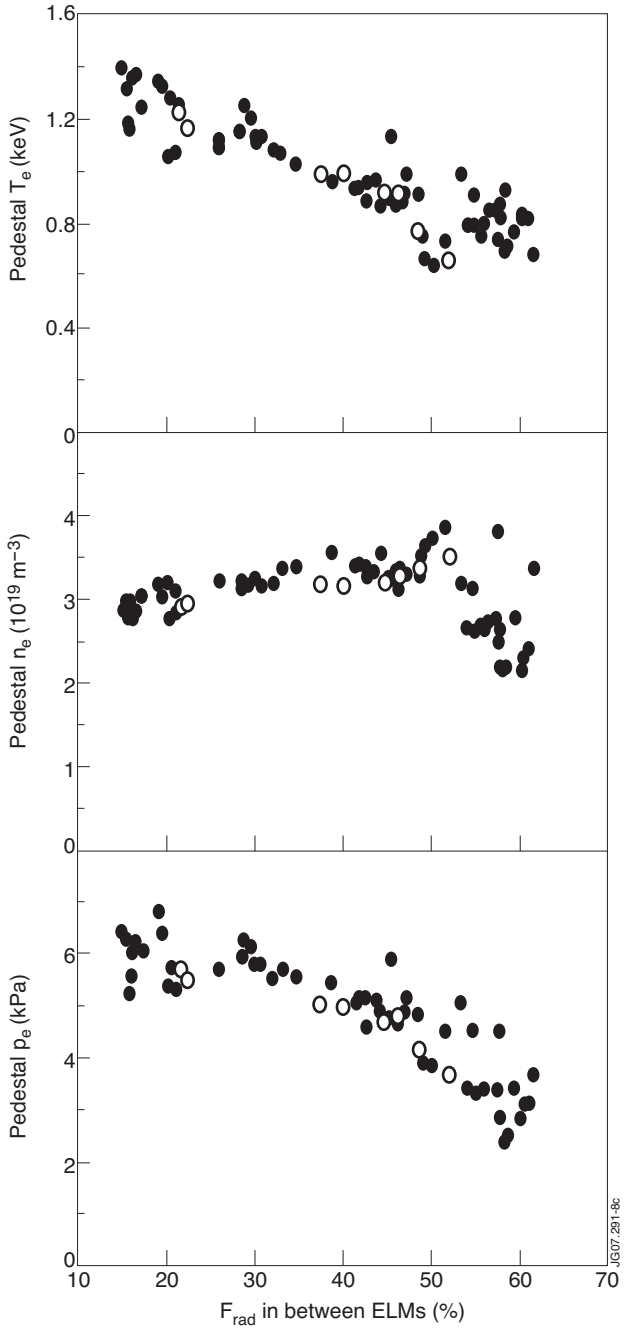

Figure 9: Pedestal T_e (ECE radiometer at r/a=0.9), n_e (Interferometry, line average over r/a>0.9) and p_e (combination of the two) versus F_{rad}. Closed symbols N_e, open symbols N_2.

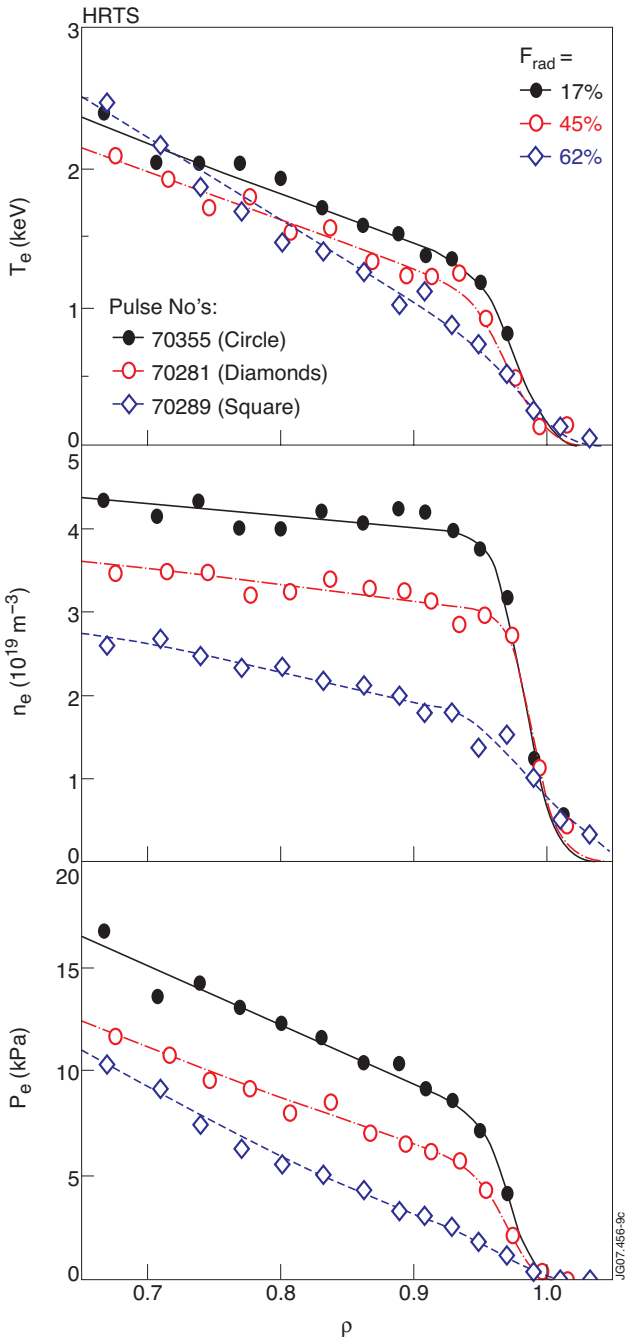

Figure 10: T_e, n_e and p_e pedestal profiles measured using the new High Resolution Thomson Scattering (HRTS) system. Profiles are averaged over 4 profile measurements, selected to be just before four individual ELMs (black and red case). (The HRTS measurement-repetition rate is 20Hz, and 10 measurements were taken per discharge, covering a time window of 0.5s). The system was not available for all discharges in the experiments reported in this paper, but a systematic dependence of the pedestal profiles on F_{rad} is observed. The solid lines are modified tanh fits.

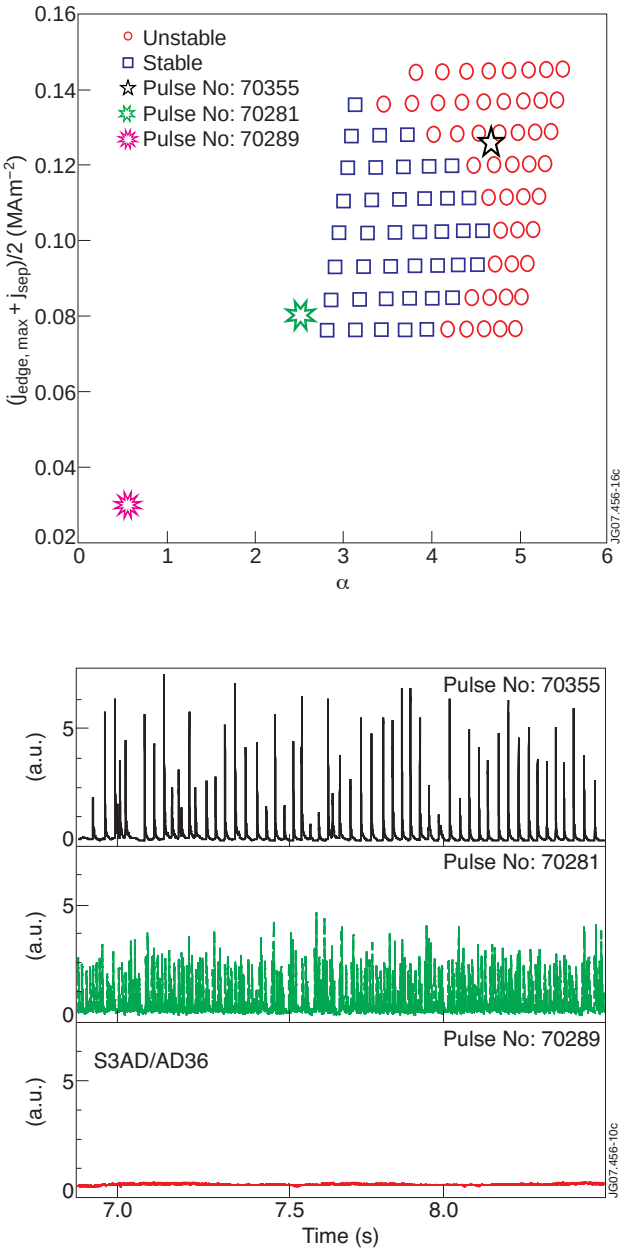

Figure 11 (a): Edge stability analysis using the ELITE code and data from the high resolution Thomson scattering system shows that at F_{rad} = 17% the plasma is marginally unstable to peeling-ballooning modes, whereas at F_{rad} = 45% and 60% the edge is in the stable domain. HRTS profile measurements used for this calculation were taken between 7 and 7.5s. (b) D_α time traces for the three different pulses. The colours match those to indicate the three different stability points in Fig.11(a)

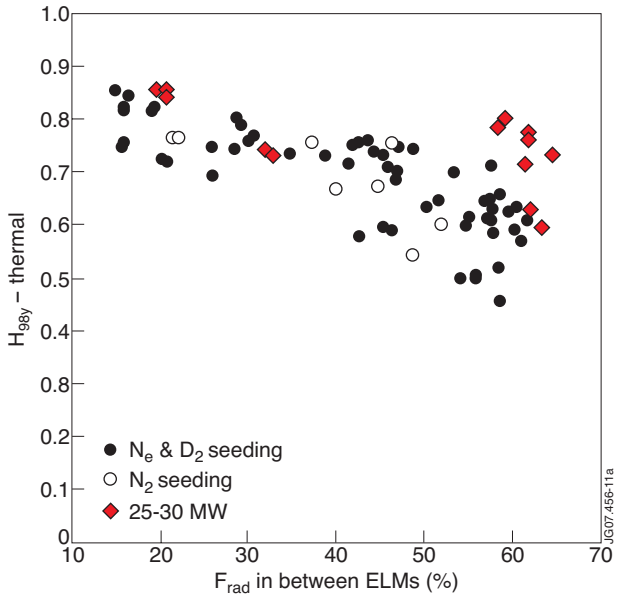

Figure 12: Confinement factor HIPB98(y,2) as a function of F_{rad}. A small initial decay due to the increase in gas fuelling is followed by a constant H98IPB(y,2) as F_{rad} is further increased until a second phase of confinement degradation takes place at F_{rad}~40-50% due to a type I – type III ELM transition. The black dots represent the data-set used elsewhere in this paper, with P_{tot} = 20-25MW, and the red diamonds have P_{tot} =25-30MW. Open symbols are N_2 seeded data.

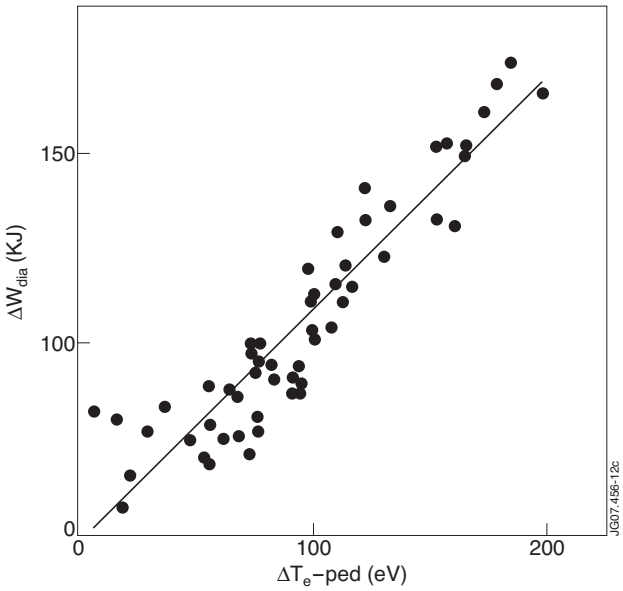

Figure 13: The linear relation between averaged ΔW_{ELM} from diamagnetic measurements and averaged ΔT_e per ELM at r/a=0.9 from Electron Cyclotron Emission (ECE) averaged over all ELMs in a ~1s wide time window per data point in the figure.

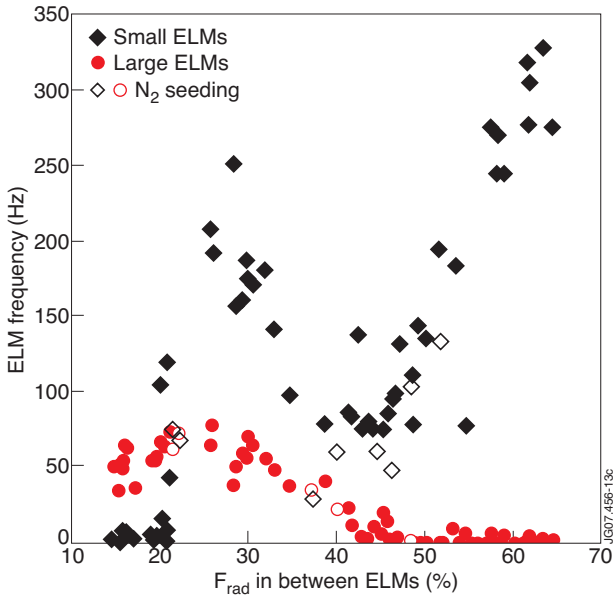

Figure 14: ELM frequency as a function of $F_{rad.}$ The ELMs have been categorised as red: 'large ELMs' (ΔT_e>75eV) and blue: 'small ELMs' (ΔT_e<75 eV). Open symbols are nitrogen seeded plasmas.

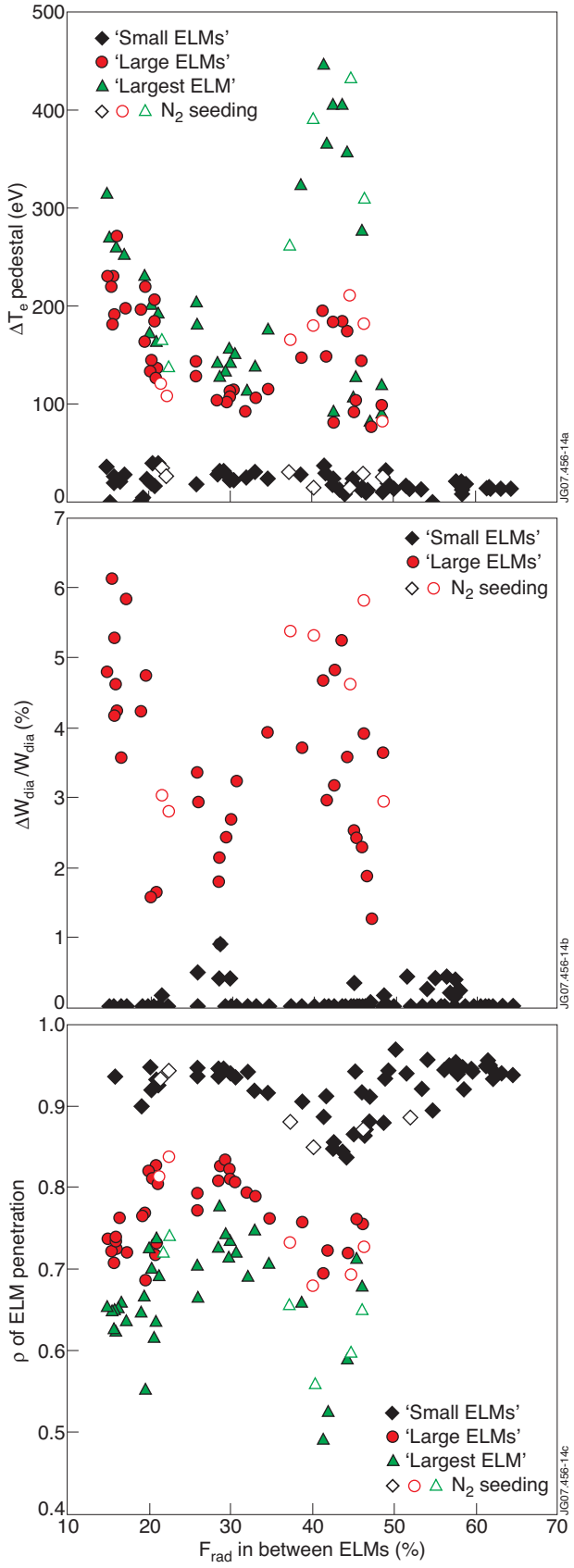

Figure 15: (a) Electron temperature drop (ΔT_e), (b) normalised W_{dia} drop ($\Delta W_{ELM}/W_{dia}$) and (c) ELM affected area expressed in ELM penetration radius (r=r/a) as a function of F_{rad}. The data for the 'small' and 'large ELMs' are ELM averaged within their category

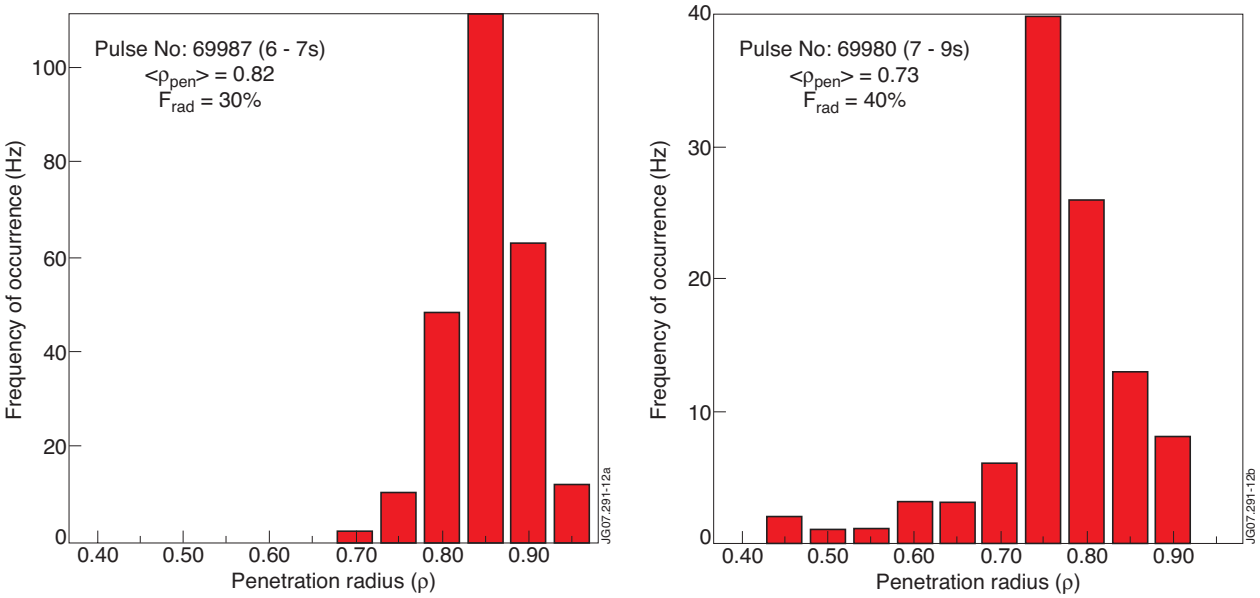

Figure 16: Distribution functions of ELM penetration depth (r=r/a) for (a) F_{rad} =30% and (b) 40%, respectively. Clearly the ELMs do not affect regions inside r/a = 0.7 for F_{rad} = 30%, whilst for F_{rad} = 40%, effects are felt at the rate of several events per second (6-10Hz).